

# A NEW FRAMEWORK FOR INCORPORATING APPEARANCE AND SHAPE FEATURES OF LUNG NODULES FOR PRECISE DIAGNOSIS OF LUNG CANCER

Ahmed Shaffie<sup>1,2\*</sup>, Ahmed Soliman<sup>1\*</sup>, Mohammed Ghazal<sup>1,3</sup>, Fatma Taher<sup>4</sup>, Neal Dunlap<sup>5</sup>,  
Brian Wang<sup>5</sup>, Adel Elmaghraby<sup>2</sup>, Georgy Gimel'farb<sup>6</sup> and Ayman El-Baz<sup>1†</sup>

<sup>1</sup>BioImaging Laboratory, Bioengineering Department, University of Louisville, Louisville, KY, USA.

<sup>2</sup>Computer Engineering and Computer Science Department, University of Louisville, Louisville, KY, USA.

<sup>3</sup>Department of Electrical and Computer Engineering, Abu Dhabi University, Abu Dhabi, UAE

<sup>4</sup>Department of Electrical and Computer Engineering, Khalifa University, Abu Dhabi, UAE

<sup>5</sup>Department of Radiation Oncology, University of Louisville, Louisville, KY, USA.

<sup>6</sup>Department of Computer Science, University of Auckland, Auckland, New Zealand.

## ABSTRACT

This paper proposes a novel framework for the classification of lung nodules using computed tomography (CT) scans. The proposed framework is based on the integrating the following features to get accurate diagnosis of detected lung nodules: (i) Spherical Harmonics-based shape features that have the ability to describe the shape complexity of the lung nodules; (ii) Higher-Order Markov Gibbs Random Field (MGRF)-based appearance model that has the ability to describe the spatial inhomogeneities in the lung nodule; and (iii) volumetric features that describe the size of lung nodules. To accurately model the surface/shape of the detected lung nodules, we used spherical harmonics expansion due to its ability to approximate the surfaces of complicated shapes. We will use the reconstruction error curve as a new metric to describe the shape complexity of the detected lung nodules. Moreover, we developed a new higher 7<sup>th</sup>-order MGRF model that has the ability to model the existing the spatial inhomogeneities for both small and large detected lung nodules. Finally, a deep autoencoder (AE) classifier is fed by the above three features to distinguish between the malignant and benign nodules. To evaluate the proposed framework, we used the publicly available data from the Lung Image Database Consortium (LIDC). We used a total of 116 nodules that were collected from 60 patients. By achieving a classification accuracy of 96.00%, the proposed system demonstrates promise to be a valuable tool for the detection of lung cancer.

**Index Terms**—Computed Tomography, Higher-order MGRF, Spherical Harmonics, Computer Aided Diagnosis

## 1. INTRODUCTION

Lung cancer is considered the leading cause of cancer death among both genders in the United States with about 1 out of 4 cancer deaths resulting from lung cancer [1]. Although there are several imaging modalities used for the diagnosis of lung cancer, e.g., magnetic resonance imaging (MRI), chest radiograph (X-ray), and many other modalities, computed tomography (CT) imaging is the most common and appropriate modality for examining the lung tissues due to its high resolution and clear contrast compared to other techniques [2–6]. Recently, the number of lung cancer cases have increased exponentially, and its early detection

can increase the chance of survival [7, 8]. Furthermore, an automated assistive tool for the radiologists is of great importance to help in the analysis of the large amount of data available from CT scans. Thus, the computer aided diagnosis systems (CADx) is of great interest and high importance. Recently, a plethora of methods for automated diagnosis of pulmonary nodules in CT scans have been introduced. Various researchers have used image processing and data mining techniques to diagnose the pulmonary nodules. Namely, Macedo et al. [9] have proposed the use of different classifiers, such as the support vector machine (SVM), and rule-based system, to distinguish between malignant and benign lung nodules. They used texture, shape, and appearance features that were extracted from the histogram of oriented gradient (HOG) from the region of interest (ROI). Kumar et al. [10] used deep features extracted from multi-layer autoencoders for the classification of lung nodules. Although they have proved the effectiveness of extracting high-level features from the input data in their experiments, they disregarded the morphological information, e.g., perimeter, skewness, and circularity of the nodule, which could not be extracted by the conventional deep models. Jia et al. [11] have proposed a rule-based classification system based on growth rate changes and registration technique. Lee et al. [12] have proposed a lung nodule classification system using a random forest classifier aided by clustering. After they merged all the data, they divided it into two clusters, then divided each cluster into two groups, nodule and non-nodule, based on the training set labels. Finally, a random forest classifier was trained for each cluster to distinguish between benign and malignant nodules. Farahani et al. [13] have proposed an ensemble-based system to classify each pulmonary nodule by integrating multiple classifiers like SVM, K-nearest-neighbors ( $k$ -NN), and neural networks. The classifiers have learned over five morphological features and the output of these classifiers is combined using majority voting. Huang et al. [14] have proposed a system to differentiate malignant from benign pulmonary nodules based on fractal texture features from Fractional Brownian Motion (FBM) model using SVM. Elsayed et al. [15] have proposed a system that uses different classifiers, e.g., Linear, Quadratic, Parzen, Neural Networks, and their different combinations such as mean, median, maximum, minimum, and voting, to enhance the performance of the classification of malignant and benign pulmonary nodules. Kim et al. [16] have proposed a system which uses a deep neural network to extract abstract information inherent in raw hand-crafted imaging features. Then, the learned representation is used

\*Equal Contribution - First Authorship

†Corresponding author, e-mail: aselba01@louisville.edu.

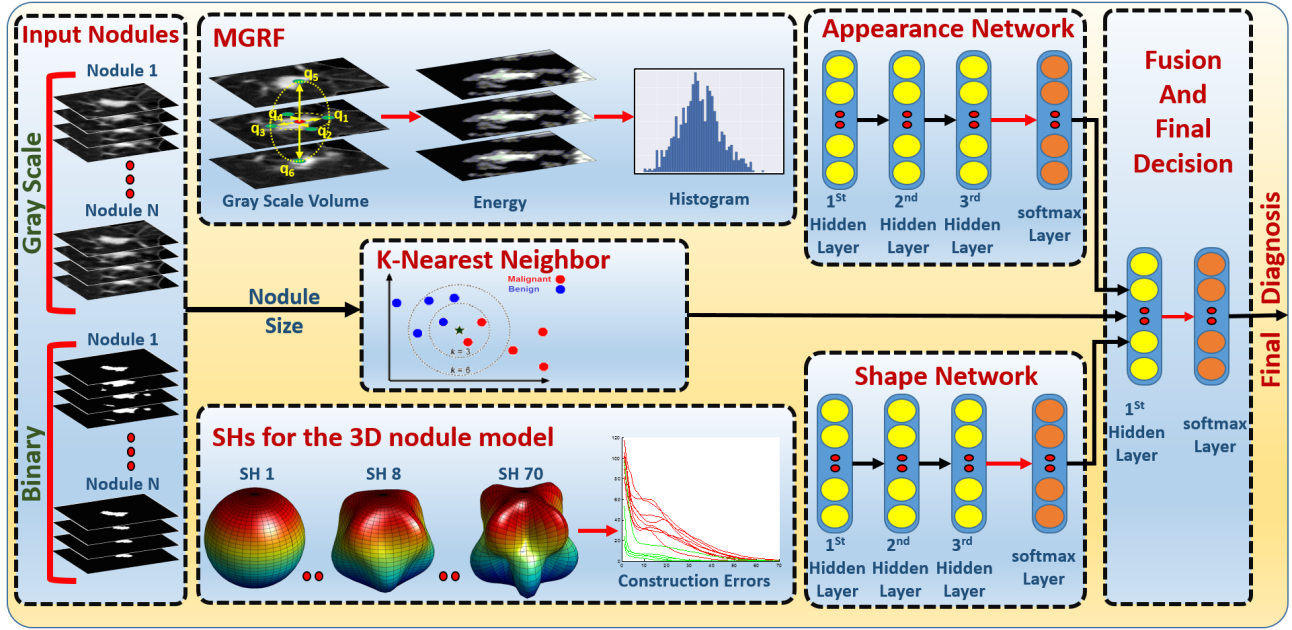


Fig. 1: Lung nodule classification framework.

with the raw imaging features to train the classifier. Narayanan et al. [17] also used deep neural network to classify the pulmonary nodules after training on morphological features.

The existing methods for the classification of lung nodules have the following limitations: (i) some methods depend on the Hounsfield Unit (HU) values as the appearance descriptor without taking any spatial interaction into consideration; (ii) methods that depend on traditional shape features are very sensitive to prior steps, e.g., segmentation. (iii) some of the methods just depend on raw data and disregard the morphological information.

To overcome these limitations, we proposed a new nodule classification framework that integrates a novel appearance feature using 7<sup>th</sup>-order MGRF that take into account 3D spatial interaction between nodule's voxels, and a geometrical shape feature using spherical harmonics analysis, for the decomposition of nodules using different SHs, with the deep autoencoder to achieve high classification accuracy.

## 2. METHODS

The proposed framework for lung nodules classification from CT scans, Fig. 1, performs four basic steps: (i) extraction of geometric shape features in terms of construction error of modeled spherical harmonics; (ii) extraction of appearance features in terms of Gibbs energy that is modeled using the 7<sup>th</sup>-order MGRF; (iii) extraction of a size feature using the  $k$ -NN classifier; (iv) nodule classification using deep autoencoder networks. Details of the framework's main components are given below.

### 2.1. Appearance features using MGRF energy

Because the spatial distribution of the Hounsfield values varies between different nodule types, less smooth for malignant nodules compared to benign, describing these visual appearance peculiarities using the MGRF model will provide discriminatory features between malignant and benign nodules (see Fig. 2).

To describe the texture appearance of the lung nodules, we calculated the Gibbs energy values using the 7<sup>th</sup>-order MGRF model, in order to use them as descriptive values to discriminate between malignant and benign ones, as these values represent the interactions between each voxel and its neighborhood [18]. Let  $\mathbb{Q} = \{0, \dots, Q - 1\}$ ; denote a finite set of signals (HU values) in the lung CT scan,  $s : \mathbb{R}^3 \rightarrow \mathbb{Q}$ , with signals  $\mathbf{s} = [s(x, y, z) : (x, y, z) \in \mathbb{R}^3]$ . The interaction graph,  $\Gamma = (\mathbb{R}^3, \mathbb{E})$ , quantifies the signal probabilistic dependencies in the images with nodes at voxels,  $(x, y, z) \in \mathbb{R}^3$ , that are connected with edges  $((x, y, z), (x', y', z')) \in \mathbb{E} \subseteq \mathbb{R}^3 \times \mathbb{R}^3$ .

An MGRF of images is defined by a Gibbs probability distribution (GPD),  $\Upsilon = [\Upsilon(\mathbf{s}) : \mathbf{s} \in \mathbb{Q}^{|\mathbb{R}|}; \sum_{\mathbf{s} \in \mathbb{Q}^{|\mathbb{R}|}} \Upsilon(\mathbf{s}) = 1]$ , factored over a set  $\mathcal{C}$  of cliques in  $\Gamma$  supporting non-constant factors, logarithms of which are Gibbs potentials [19, 20]. To make modeling more efficient at describing the visual appearance of different nodules in the lung CT scans, the 7<sup>th</sup>-order MGRF models the voxel's partial ordinal interaction within a radius  $r$  rather than modeling the pairwise interaction as in the 2<sup>nd</sup>-order MGRF.

Let a translation-invariant 7<sup>th</sup>-order interaction structure on  $\mathbb{R}$  be represented by  $A$ ,  $A \geq 1$ , families,  $\mathcal{C}_a$ ;  $a = 1, \dots, A$ , of 7<sup>th</sup>-order cliques,  $\mathbf{c}_{a:x,y,z} \in \mathcal{C}_a$ , of the same shape and size. Every clique is associated with a certain voxel (origin),  $(x, y, z) \in \mathbb{R}$ , supporting the same (7)-variate scalar potential function,  $V_a : \mathbb{Q}^7 \rightarrow (-\infty, \infty)$ . The Gibbs probability distribution for this contrast/offset-, and translation-invariant MGRF is

$$\Upsilon_7(\mathbf{s}) = \frac{1}{Z} \phi(\mathbf{s}) \exp(-E_7(\mathbf{s})) \quad (1)$$

where  $E_{7;a}(\mathbf{s}) = \sum_{\mathbf{c}_{a:x,y,z} \in \mathcal{C}_a} V_{7;a}(g(x', y', z') : (x', y', z') \in \mathbf{c}_{a:x,y,z})$  and  $E_7(\mathbf{s}) = \sum_{a=1}^A E_{7;a}(\mathbf{s})$  denote the Gibbs energy for each individual, and all the clique families, respectively;  $Z$  is a normalization factor, while  $\phi(\mathbf{s})$  is a core distribution. The calculated Gibbs energy,  $E_7(\mathbf{s})$ , will be used to discriminate between benign and malignant tissues and gives an indication of malignancy. While a high potential of malignancy is indicated by higher energy, high potential to be benign is indicated by lower energy. To calculate  $E_7(\mathbf{s})$ , the Gibbs potentials for the 7<sup>th</sup>-order model

are calculated using the maximum likelihood estimates (MLE) by generalizing the analytical approximation in [21, 22]:

$$V_{7:a}(\xi) = \frac{F_{7:a:\text{core}}(\xi) - F_{7:a}(\xi|\mathbf{s}^\circ)}{F_{7:a:\text{core}}(\xi)(1 - F_{7:a}(\xi|\mathbf{s}^\circ))}; \quad a = 1, \dots, A; \quad \xi \in \vartheta_7$$

where  $\mathbf{s}^\circ$  denoted the training malignant nodule images;  $\xi$  denotes a numerical code of a particular 7<sup>th</sup>-order relation between the 7 signals on the clique;  $\vartheta_7$  is a set of these codes for all 7<sup>th</sup>-order signal co-occurrences;  $F_{7:a}(\mathbf{s}^\circ)$  is an empirical marginal probability of the relation  $\xi$ ;  $\xi \in \vartheta_7$ , over the 7<sup>th</sup>-order clique family  $\mathbb{C}_{7:a}$  for  $\mathbf{s}^\circ$ , and  $F_{7:a:\text{core}}(\xi)$  is the core probability distribution.

## 2.2. Spherical harmonics (SHs) shape analysis

To model the lung nodules using Spectral SH analysis [23], their 3D surface is considered a linear combination of specific basis functions. First, a triangulated 3D mesh, built with an algorithm by Fang and Boas [24], is used to approximate the nodules 3D surface. Secondly, the lung nodule surface is mapped for the SH decomposition to the unit sphere. To provide a more accurate modeling for the nodule geometry, we used our developed mapping approach, the Attraction-Repulsion Algorithm, that preserves two conditions: (i) the distance of each node to the nodule center is unity, and (ii) the distance of each node to all of its neighbors is equal, as shown in Fig. 4. Let  $I$  denote total number of mesh nodes,  $\alpha$  be the iteration index, and  $\mathbf{C}_{\alpha,i}$  be the 3D coordinates of the surface node  $i$  at iteration  $\alpha$ ;  $i = 1, \dots, I$ . Let  $J$  be the number of the mesh node neighbors (as shown in Fig. 4) and  $d_{\alpha,j}$  denote the Euclidean distance between  $i$  and  $j$  at iteration  $\alpha$  (as shown in Fig. 4(b)), where  $j = 1, \dots, J$ . Let  $\mathbf{d}_{\alpha,ji} = \mathbf{C}_{\alpha,j} - \mathbf{C}_{\alpha,i}$  denote the displacement between the nodes  $j$  and  $i$  at iteration  $\alpha$ . Let  $C_{A,1}$ ,  $C_{A,2}$ ,  $C_R$  be the constants for attraction and repulsion, that control each surface node displacement. The starting attraction step of the proposed mapping tends to center each node  $\mathbf{C}_i$ ; with respect to its neighbors by iteratively adjusting its location:

$$\mathbf{C}'_{\alpha,i} = \mathbf{C}_{\alpha,i} + C_{A,1} \sum_{j=1:j \neq i}^J \mathbf{d}_{\alpha,ji} d_{\alpha,ji}^2 + C_{A,2} \frac{\mathbf{d}_{\alpha,ji}}{d_{\alpha,ji}} \quad (2)$$

The adjusted nodes are pushed away from their neighbors if they are much closer than others, and the tightly packed nodes are kept from collision using the  $C_{A,2}$  factor. Subsequently, the whole mesh is inflated in the repulsion step by pushing all the nodes outward to preserve the equi-spaced condition after their final back-projection onto the unit sphere along the rays from the center of the sphere. Each  $\mathbf{C}_i$  location is updated before the back-projection to avoid the collision between nodes that have not shifted and the altered ones, as follows:

$$\mathbf{C}^{\circ}_{\alpha+1,i} = \mathbf{C}'_{\alpha,i} + \frac{C_R}{2I} \sum_{j=1:j \neq i}^I \left( \frac{\mathbf{d}_{\alpha,ji}}{|\mathbf{d}_{\alpha,ji}|^2} \right) \quad (3)$$

where a repulsion constant  $C_R$  controls the displacement of each surface node and provides a balance between the accuracy and processing time (e.g. a smaller  $C_R$  value guarantees high accuracy at the expense of the increased processing time). All the experiments below were obtained with  $I = 4896$  nodes and  $0.3 \leq C_R \leq 0.7$ .

After mapping the original lung nodule to the unit sphere using the proposed algorithm, it will be approximated by a linear combination of SHs. To represent more generic information (e.g., benign nodules), a lower-order harmonics will be sufficient; while higher-order harmonics are required for finer details (e.g., malignant nodules). The SHs coefficients are generated by solving an isotropic heat equation for the nodule surface on the unit sphere [23].

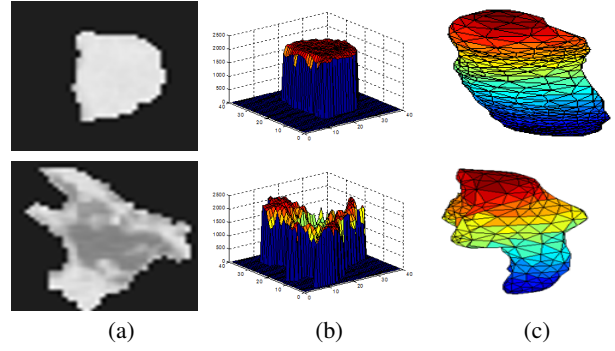


**Fig. 2:** Benign (*first-row*) and malignant (*second-row*) lung nodules (a), along their 3D visualization of Hounsfield values (b), and 3D mesh visualization (c).

Finally, the generated SHs coefficients are used to reconstruct the lung nodule. The iterative residual fitting by Shen and Chung [25] has been used to approximate the 3D shape of modeled nodules. Figure 3 demonstrates that there is no significant change in the model accuracy for benign nodules from 15 to 70 SHs, while it continues to change for malignant ones.

Due to the small dimensionality of the size feature, we used a simple  $k$ NN classifier as a probability estimator to determine each class (benign or malignant) membership for each nodule.

## 2.3. Nodule classification using autoencoders

To classify the pulmonary lung nodules, our CADx system uses a deep neural network with a two-stage structure of stacked autoencoder (AE). In the first stage, two autoencoder-based classifiers, one classifier for the appearance and the other one for the shape, are employed to estimate initial classification probabilities that are chained together with output probabilities of the  $k$ -NN classification. The chained probabilities will be the input for the second stage autoencoder to estimate the final classification (see Fig. 1 for more details). AE is used to reduce the dimensionality of the input data (70 error features for the shape network and 200 histogram bins for the Gibbs energy image in the appearance network) with multi-layered neural networks to catch the most distinguishing features by greedy unsupervised pre-training. A softmax output layer is stacked after the AE layers to enhance the classification by minimizing the total loss for the training labeled data. For each AE, let  $W = \{W_j^e, W_i^d : j = 1, \dots, s; i = 1, \dots, n\}$  refer to a set of column vectors of weights for encoding,  $E$ , and decoding,  $D$ , layers, and let  $T$  denote vector transposition. The AE change the  $n$ -dimensional column vector  $u = [u_1, \dots, u_n]^T$  into an  $s$ -dimensional column vector  $h = [h_1, \dots, h_s]^T$  of hidden features such that  $s < n$  by nonlinear uniform transformation of  $s$  weighted linear combinations of input as  $h_j = \sigma((W_j^e)^T u)$  where  $\sigma(\cdot)$  is a sigmoid function with values from  $[0, 1]$ ,  $\sigma(t) = \frac{1}{1+e^{-t}}$ . Our classifier is constructed by stacking AE which consist of 3 hidden layers with softmax layer. The first hidden layer reduces the input vector to 50 level activators, while the second hidden layer continues the reduction to 30 level activators which are reduced to 10 after the third layer. The 10 level activators are the input to the softmax layer which compute the probability of being malignant or benign through the following equation:-

$$p(c; W_{o:c}) = \frac{e^{(W_{o:c}^T h^3)}}{e^{(\sum_1^C W_{o:c}^T h^3)}} \quad (4)$$

Where  $C = 1, 2$ ; denote the class number  $W_{o:c}$ : is the weight vector for the softmax for class  $c$ ;  $h^3$ : are the output features

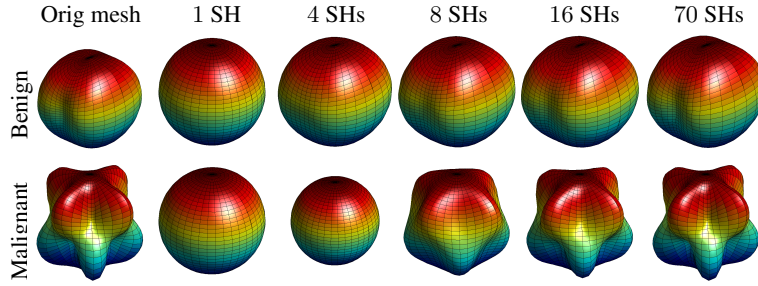


**Fig. 3:** Benign (*first-row*) and malignant (*second-row*) nodules shape approximation.

from the last hidden layer, (the third layer), of the AE. In the second stage, the output probability obtained from the softmax of the appearance and shape networks, are fused together with the size probability, obtained from the  $k$ -NN, and fed to another AE which comprised of 1 hidden layer followed by softmax layer to give the final classification probability.

### 3. EXPERIMENTAL RESULTS AND CONCLUSION

To test the proposed CADx system, we used the publicly available dataset from the Lung Image Database Consortium (LIDC) [26], which is considered one of the largest publicly available databases. This dataset comprises of diagnostic and lung cancer screening thoracic computed tomography (CT) scans augmented with XML files to give a full description about the annotated lesions and mark them up. The annotation and malignancy scoring process is performed by four experienced radiologists in two phases; the first phase is blinded-read for each radiologist independently of the other radiologists; the second phase is unblinded-read phase in which the radiology gives his final decision after reviewing the three radiologists' opinions. The lesions are divided by each radiologist to nodules, and non-nodule, and every nodule takes a malignancy score that ranges from 1, benign, to 5, malignant. The total number of extracted nodules is 116 (75 benign and 41 malignant), collected from 60 patients. Each nodule is extracted within a volume-of-interest (VOI) of size  $40 \times 40 \times 40$  mm, from the nodule center and its mask is obtained by calculating the overlap between the four radiologists' delineation. The final diagnosis for each nodule is calculated as the average score for the four radiologists, and to give the training phase more confidence, we used only the high confidence malignant/benign scores, in other words, we used the nodules which get consist scoring across the four radiologists. In order to evaluate our system and highlight the merit of using that system, we used the "leave-one-subject-out" cross-validation procedure. The classification accuracy has been reported in terms of four measures, namely, the sensitivity, specificity, accuracy, and the area under the curve (AUC) of the receiver operating characteristics (ROC). To highlight each feature contribution, we evaluated the accuracy of our deep network components; the shape, appearance, and size networks, in addition to the complete fused system. Table 1 shows the evaluation metrics for every module and for the whole system after the fusion process. It is clear that the modeled features gives a good discrimination between benign and malignant nodules, moreover, the discrimination accuracy is very high when all these features are fused together using the deep AE. Furthermore, Fig. 5 shows the ROC, which tests the sensitivity of our framework against the selected operating points (classification thresholds) for the used features and their final fusion.

To highlight the advantages behind using deep AE, we com-

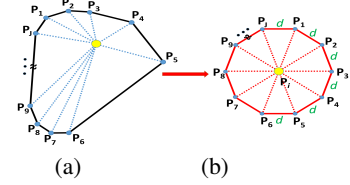


**Fig. 4:** Illustration of the neighbors rearrangement (in 2D projection): initial (a) vs. final equidistant locations (b).

**Table 1:** Classification results; in terms of Sensitivity, Specificity, Accuracy, and AUC; for different feature groups.

	Evaluation Metrics			
	Sens.	Spec.	Acc.	AUC
Size	91.67	79.35	81.90	80.03
Shape	80.43	94.29	88.79	93.07
Appearance	81.58	87.18	85.34	90.57
Comb. Features	<b>90.48</b>	<b>95.95</b>	<b>93.97</b>	<b>96.00</b>

**Table 2:** Classification results for the deep autoencoder classifier compared with RF and SVM classifiers.

	Classifier Type		
	AE	RF	SVM
Sens.	<b>90.48</b>	93.30	90.70
Spec.	<b>95.95</b>	80.50	73.20
Acc.	<b>93.97</b>	88.79	84.48
AUC	<b>96.00</b>	95.10	81.90

pared the classification accuracy for the fused features using the deep AE, RandomForest (RF), and the support vector machine (SVM) classifiers. Table 2 shows that the deep AE achieves the highest accuracy among all other classifiers. In conclusion, this

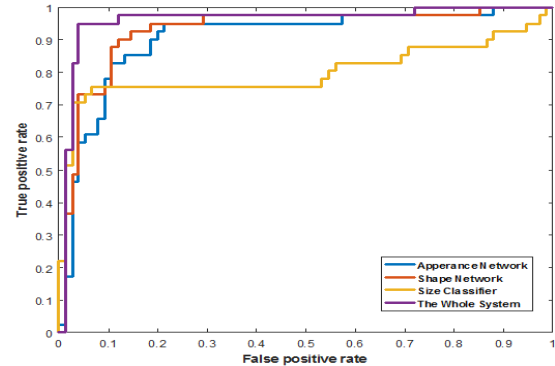


**Fig. 5:** Classification accuracy for different features.

paper introduced a novel framework for the classification of lung nodules by modeling geometrical and appearance features. The classification results obtained from a set of 116 nodules collected from 60 patients confirm that the proposed framework holds the promise for the detection of lung cancer. This promising results encourage us to file an IRB protocol in the future and locally collect data at our site to test on subjects that have malignant/benign nodules with biopsy confirmation.

**Acknowledgment:** This research work has been supported by Research Grant from the Kentucky Lung Cancer Research Program.

#### 4. REFERENCES

- [1] American Cancer Society, "Cancer Facts and Figures," 2016.
- [2] D. Karthikeyan and D. Chegu, *High-resolution Computed Tomography of the Lungs: A Pattern Approach*, 2004.
- [3] A. Soliman, F. Khalifa, A. Elnakib, M. A. El-Ghar, N. Dunlap, B. Wang, G. Gimelfarb, R. Keynton, and A. El-Baz, "Accurate lungs segmentation on CT chest images by adaptive appearance-guided shape modeling," *IEEE Transactions on Medical Imaging*, vol. 36, no. 1, pp. 263–276, 2017.
- [4] A. Soliman, A. Elnakib, F. Khalifa, M. A. El-Ghar, and A. El-Baz, "Segmentation of pathological lungs from CT chest images," in *2015 IEEE International Conference on Image Processing (ICIP)*. IEEE, 2015, pp. 3655–3659.
- [5] A. El-Baz, G. M. Beache, G. Gimelfarb, K. Suzuki, K. Okada, A. Elnakib, A. Soliman, and B. Abdollahi, "Computer-aided diagnosis systems for lung cancer: challenges and methodologies," *International journal of biomedical imaging*, vol. 2013, 2013.
- [6] A. Soliman, F. Khalifa, A. Alansary, G. Gimelfarb, and A. El-Baz, "Segmentation of lung region based on using parallel implementation of joint mrf: Validation on 3d realistic lung phantoms," in *2013 IEEE 10th International Symposium on Biomedical Imaging (ISBI)*. IEEE, 2013, pp. 864–867.
- [7] T. W. Way, B. Sahiner, H.-P. Chan, L. Hadjiiski, P. N. Cascade, A. Chughtai, N. Bogot, and E. Kazerooni, "Computer-aided diagnosis of pulmonary nodules on CT scans: improvement of classification performance with nodule surface features," *Medical physics*, vol. 36, no. 7, pp. 3086–3098, 2009.
- [8] B. Abdollahi, A. Soliman, A. Civelek, X.-F. Li, G. Gimelfarb, and A. El-Baz, "A novel 3d joint mrf framework for precise lung segmentation," in *International Workshop on Machine Learning in Medical Imaging*. Springer, 2012, pp. 86–93.
- [9] M. Firmino, G. Angelo, H. Morais, M. R. Dantas, and R. Valentim, "Computer-aided detection (CAdE) and diagnosis (CAdx) system for lung cancer with likelihood of malignancy," *Biomedical engineering online*, vol. 15, no. 1, pp. 2, 2016.
- [10] D. Kumar, A. Wong, and D. A. Clausi, "Lung nodule classification using deep features in ct images," in *2015 12th Conference on Computer and Robot Vision (CRV)*. IEEE, 2015, pp. 133–138.
- [11] T. Jia, Y. Bai, H. Zhang, D. Chen, X. Yu, and C. Wu, "Lung nodules classification based on growth changes and registration technology," in *2016 Chinese Control and Decision Conference (CCDC)*. IEEE, 2016, pp. 5359–5364.
- [12] S. L. A. Lee, A. Z. Kouzani, and E. J. Hu, "Random forest based lung nodule classification aided by clustering," *Computerized medical imaging and graphics*, vol. 34, no. 7, pp. 535–542, 2010.
- [13] F. V. Farahani, A. Ahmadi, and M. F. Zarandi, "Lung nodule diagnosis from CT images based on ensemble learning," in *2015 IEEE Conference on Computational Intelligence in Bioinformatics and Computational Biology (CIBCB)*. IEEE, 2015, pp. 1–7.
- [14] P.-W. Huang, P.-L. Lin, C.-H. Lee, and C. Kuo, "A classification system of lung nodules in CT images based on fractional brownian motion model," in *System Science and Engineering (ICSSE), 2013 International Conference on*. IEEE, 2013, pp. 37–40.
- [15] O. Elsayed, K. Mahar, M. Kholief, and H. A. Khater, "Automatic detection of the pulmonary nodules from CT images," in *SAI Intelligent Systems Conference (IntelliSys), 2015*. IEEE, 2015, pp. 742–746.
- [16] B.-C. Kim, Y. S. Sung, and H.-I. Suk, "Deep feature learning for pulmonary nodule classification in a lung CT," in *2016 4th International Winter Conference on Brain-Computer Interface (BCI)*. IEEE, 2016, pp. 1–3.
- [17] J. Jeeva et al., "A computer aided diagnosis for detection and classification of lung nodules," in *2015 IEEE 9th International Conference on Intelligent Systems and Control (ISCO)*.
- [18] N. Liu, A. Soliman, G. Gimelfarb, and A. El-Baz, "Segmenting kidney DCE-MRI using 1st-order shape and 5th-Order appearance priors," in *International Conference on Medical Image Computing and Computer-Assisted Intervention*. Springer, 2015, pp. 77–84.
- [19] A. Soliman, F. Khalifa, A. Shaffie, N. Liu, N. Dunlap, B. Wang, A. Elmaghraby, G. Gimelfarb, and A. El-Baz, "Image-based CAD system for accurate identification of lung injury," in *2016 IEEE International Conference on Image Processing (ICIP)*. IEEE, 2016, pp. 121–125.
- [20] A. Soliman, F. Khalifa, A. Shaffie, N. Dunlap, B. Wang, A. Elmaghraby, and A. El-Baz, "Detection of lung injury using 4D-CT chest images," in *2016 IEEE 13th International Symposium on Biomedical Imaging (ISBI)*. IEEE, 2016, pp. 1274–1277.
- [21] G. Gimelfarb and A. Farag, "Texture analysis by accurate identification of simple markovian models," *Cybernetics and Systems Analysis*, vol. 41, no. 1, pp. 27–38, 2005.
- [22] A. El-Baz, G. Gimelfarb, and J. S. Suri, *Stochastic modeling for medical image analysis*, CRC Press, 2015.
- [23] A. El-Baz, M. Nitzken, F. Khalifa, A. Elnakib, G. Gimelfarb, R. Falk, and M. A. El-Ghar, "3D shape analysis for early diagnosis of malignant lung nodules," in *Biennial International Conference on Information Processing in Medical Imaging*. Springer, 2011, pp. 772–783.
- [24] Q. Fang and D. A. Boas, "Tetrahedral mesh generation from volumetric binary and grayscale images," in *Biomedical Imaging: From Nano to Macro, 2009. ISBI'09. IEEE International Symposium on*. IEEE, 2009, pp. 1142–1145.
- [25] M. K. Chung et al., "Weighted fourier series representation and its application to quantifying the amount of gray matter," *IEEE transactions on medical imaging*, vol. 26, no. 4, pp. 566–581, 2007.
- [26] S. G. Armato, G. McLennan, L. Bidaut, M. F. McNitt-Gray, C. R. Meyer, A. P. Reeves, B. Zhao, D. R. Aberle, C. I. Henschke, E. A. Hoffman, et al., "The lung image database consortium (LIDC) and image database resource initiative (IDRI): a completed reference database of lung nodules on CT scans," *Medical physics*, vol. 38, no. 2, pp. 915–931, 2011.